Scripta Materialia 147 (2018) 83–87

Contents lists available at ScienceDirect

Scripta Materialia

journal homepage: www.elsevier.com/locate/scriptamat

Regular article

Coherency strains of H-phase precipitates and their influence on functional properties of nickel-titanium-hafnium shape memory alloys

Behnam Amin-Ahmadi [a,*], Joseph G. Pauza [a], Ali Shamimi [b], Tom W. Duerig [b], Ronald D. Noebe [c], Aaron P. Stebner [a]

[a] Mechanical Engineering, Colorado School of Mines, Golden, CO 80401, USA
[b] Confluent Medical Technologies, Fremont, CA 94539, USA
[c] NASA Glenn Research Center, Materials and Structures Division, Cleveland, OH 44135, USA

ARTICLE INFO

Article history:
Received 8 August 2017
Received in revised form 29 December 2017
Accepted 4 January 2018
Available online xxxx

Keywords:
Aging
Transmission electron microscopy (TEM)
Geometrical phase analysis (GPA)
Precipitation
Shape memory alloys (SMA)

ABSTRACT

A $Ni_{50.3}Ti_{41.7}Hf_8$ alloy was studied after two-step aging treatments consisting of 300 °C for 12 h followed by 550 °C for different times. An anomalous change in transformation temperatures was observed as the second aging time was increased from 7.5 to 13.5 h. Initially with increased aging time (0.5–7.5 h) at 550 °C, coherency strain fields about H-phase precipitates increased. The corresponding backstress favored martensite formation, hence an increase in transformation temperatures. However, a point was eventually reached where misfit dislocations relaxed those strain fields and the effect was reduced, resulting in a decrease in transformation temperatures.

NiTiHf alloys have received considerable attention for their use as high-temperature shape memory alloys (SMAs). NiTiHf SMAs can exhibit shape memory and superelastic properties from a thermoelastic austenite–martensite transformation under temperature change or applied stress at higher temperatures than binary NiTi SMSAs (>100 °C). In compositions that are also nickel-rich (>50 at.%), these behaviors may be strongly influenced by H-phase precipitates [1–3]. The H-phase has a face-centered orthorhombic lattice, with a space group of F 2/d 2/d 2/d [1]. While the reported compositions vary, the H-phase composition is rich in Ni and Hf compared with the surrounding matrix (for example, $Ni_{50}Ti_{17}Hf_{33}$) [1,4]. Generally, an increase in Hf in NiTiHf alloys will increase transformation temperatures while an increase in nickel will decrease them. Thus, H-phase precipitation presents competing chemical effects due to the precipitates being both nickel and hafnium rich. It has been reported that the transformation temperatures in Ni-rich NiTiHf alloys generally increase with increased aging times and growth of H-phase precipitates [5–9], resulting in an understanding that the transformation temperature is more dependent on Ni content (i.e., Ni: Ti + Hf ratio) than the changes in Hf content. The exception, which is still not well understood, is aging at low temperatures for relatively short times, where transformation temperatures initially decrease before the generally observed increase [2,8].

Moreover, these fine H-phase precipitates hinder dislocation movement by increasing the critical stress necessary for slip, which leads to excellent reversibility of the martensitic transformation. Simply aging of Ni-rich $Ni_{50.3}Ti_{29.7}Hf_{20}$ has been shown to result in high strength, excellent superelasticity and actuation, and microstructural and dimensional stability when 10–20 nm H-phase precipitates are present, without any need for training; additionally, the alloy still exhibits relatively high transformation temperatures [10–12]. The operating conditions for good reversibility of the transformations of unaged alloys, however, is more limited because of their lower matrix strengths [8,13]. Therefore, the functional behavior of NiTiHf alloys in terms of transformation temperatures, transformation strain, critical martensitic transformation stress, and matrix strength can be impacted by aging heat treatments that alter H-phase morphologies. Two main factors that impact the martensitic transformation are understood to be: 1) the "mechanical effect" and 2) the "compositional effect." The former is a function of the precipitate size, interface structure, and the interparticle distance; the latter is primarily related to the composition change in the matrix due to the precipitation [2,14,15].

Precipitate strain fields and chemical gradients in the surrounding matrix impact the martensitic transformation in NiTi alloys [16,17]. When the precipitates are small and coherent, the surrounding matrix is strained to accommodate the lattice mismatch. Using geometrical phase analysis (GPA), Tirry et al. [16,18] measured the strain field (up to 2%) around coherent 50 nm Ni_4Ti_3 precipitates in NiTi alloys. These strain fields favor formation of martensite via the Clausius-Clapeyron

* Corresponding author.
E-mail addresses: baminahmadi@mines.edu, behnam.aminahmadi@gmail.com (B. Amin-Ahmadi).

https://doi.org/10.1016/j.scriptamat.2018.01.005
1359-6462/

relationship that governs the phase transformation. When the precipitates grow further in size, they lose their coherency and the strain fields are relaxed by formation of interface (misfit) dislocations along the precipitate–matrix interface; therefore, they lose their potential to affect the nucleation of martensitic phases [16,17].

The precipitates in NiTiHf alloys should also have a similar influence on the martensitic transformation. However, the exact nature of the strain fields about H-phase precipitates and their correlation to martensitic phase transformations in NiTiHf alloys has been proposed [14], but not directly observed. In the present study, the coherency and strain fields of the H-phase precipitates in $Ni_{50.3}Ti_{41.7}Hf_8$ were quantified and correlated with the martensitic transformation temperatures (TTs) and critical martensitic transformation stress.

A NiTiHf alloy with target composition of $Ni_{50.3}Ti_{41.7}Hf_8$ (at. %) was made by induction-melting high-purity elemental constituents using a graphite crucible and casting into a copper mold. The ingot was homogenized in a vacuum furnace at 1050 °C for 72 h, and were then extruded at 900 °C at a 7:1 area reduction ratio. The extruded rod was then sectioned into samples that were initially solution-annealed at 1050 °C for 30 min, water quenched, and then aged at 300 °C for 12 h and air-cooled (see ref. [3] for the effect of pre-aging treatment in NiTiHf alloys). Finally, the samples were aged a second time at 550 °C for different times (0.5, 3.5, 7.5 and 13.5 h) and air-cooled. The extruded samples were encapsulated in a quartz tube under Ar during all heat treatments.

Differential scanning calorimetry (DSC) tests were performed using a TA Instruments Q100 V9.9 with heating and cooling rates of 10 °C/min and temperature range between −180 °C and 150 °C. Mechanical compression tests were performed on a MTS test stand, and the applied force was measured using a MTS 661.20 load cell. Compression samples were cylindrical with a diameter of 5 mm and a length of 10 mm. Compression cycling for 5 cycles was applied using a maximum load of 40 kN and a minimum load of 250 N, corresponding to 2 GPa and 13 MPa compressive engineering stress limits. A speed of 0.1 mm/min was used, corresponding to approximate strain rate of $10^{-4}\ s^{-1}$.

The surfaces of the samples were speckled using an airbrush to deposit sequential layers of alumina powders (≤10 μm) and Brother TB450 carbon black toner powder. Digital images were acquired during loading, and the Ncorr Digital Image Correlation (DIC) software was used to analyze the displacements of these particles. From these displacement fields, the software calculated the surface strains during deformation. Before each test, eight images of the undeformed sample were acquired and analyzed to establish the strain noise (10^{-4} to 10^{-5}).

Conventional and high-resolution transmission electron microscopy (HRTEM) of aged NiTiHf samples was carried out using an FEI Talos TEM (FEG, 200 kV). The TEM samples were prepared by grinding the slices to 90–100 μm thick; a mechanical punch was then used to create 3 mm discs. A Fischione automatic twin-jet electropolisher (model 120) at 13 V was then used to thin the TEM foils. An electrolyte of HNO_3 and methanol in a 1:3 volume ratio at around −35 °C was used for electropolishing. To measure the size of H-phase precipitates and interparticle distance (the distance of a single precipitate from its closest precipitate), several HRTEM images taken from various regions, were used. This measurement was repeated for almost 100 precipitates on each sample and average precipitate size, average interparticle distance and their corresponding standard error is reported. Note that the interparticle distances were measured from 2D HRTEM images. Because measurements of this type can be influenced by the thickness of the TEM samples, we were careful to use only the regions of the TEM samples that were of the same thickness to measure and compare interparticle distances between different samples.

The dislocation density in the aged samples was measured by counting extra half-planes in HRTEM images. For better visualization of the extra half-planes, a mask was applied on each **g**-vector, and the corresponding inverse fast Fourier transform (IFFT) was generated showing one family of planes. This procedure was used for all main spots present in the FFT pattern; thus, the dislocation density was calculated on the basis of the number of extra half-planes present in all IFFT images. Special precaution was taken to exclude regions exhibiting "reversal of contrast" due to changes of thickness/defocus. A series of HRTEM images from a given region was thus obtained at different defocus conditions to reveal the presence of contrast reversal. Also, special attention was paid to avoid the misidentification of Moiré-effect-induced lattice image shifting as dislocations. The individual dislocation density was measured for several grains and several regions inside an individual grain for each aging time and corresponding average dislocation density and standard error was reported. To quantify the strain fields in HRTEM images, the GPA technique was used. GPA is an image-processing technique sensitive to small displacements of the lattice fringes in HRTEM images [19]. A Gaussian selection window was used in the GPA analysis with a diameter such that the spatial resolution of strain determination was 2 nm.

In studying the effect of heat treatments on functional properties of $Ni_{50.3}Ti_{29.7}Hf_{20}$, a 550 °C, 3 h aging has been shown to result in optimized strength and minimized thermal hysteresis of the martensitic transformation [7–11]. We initially tried the same heat treatment on the $Ni_{50.3}Ti_{41.7}Hf_8$ alloy, but the preliminary work found that if we first aged at 300 °C for 12 h, we achieved more superelastic transformation strain than after a direct, 1-step 550 °C age. Therefore, in the present study, the martensitic transformation temperatures and superelastic behavior of $Ni_{50.3}Ti_{41.7}Hf_8$ were studied after a multi-step heat treatment consisting of a solution anneal, a 300 °C/12 h heat treatment, and finally aging at 550 °C for various aging times. Fig. 1a shows the DSC curves of the $Ni_{50.3}Ti_{41.7}Hf_8$ alloy after aging at 550 °C for different times. The martensite start temperature (M_s) is indicated by arrows in Fig. 1a. M_s of the aged sample at 550 °C for 0.5 h is −65 °C. It increases to −34 °C and −7 °C after aging for 3.5 h and 7.5 h, respectively. However, with further aging at 550 °C for 13.5 h, the M_s then decreases to −19 °C. The A_f (Austenite finish temperature) of the aged sample at 550 °C for 0.5 h is 13 °C and increases to 22 °C and 41 °C after aging for 3.5 h and 7.5 h, respectively. Similar to the trend with M_s, with further aging at 550 °C for 13.5 h, the A_f decreases to 30 °C.

Fig. 1b shows the compression superelastic responses of the $Ni_{50.3}Ti_{41.7}Hf_8$ samples aged at 550 °C for different times. The compression tests were performed at room temperature (23 °C); therefore, all the tests except for the 550 °C/0.5 h were performed below A_f. For these tests, the unloaded strains observed at the end of each mechanical

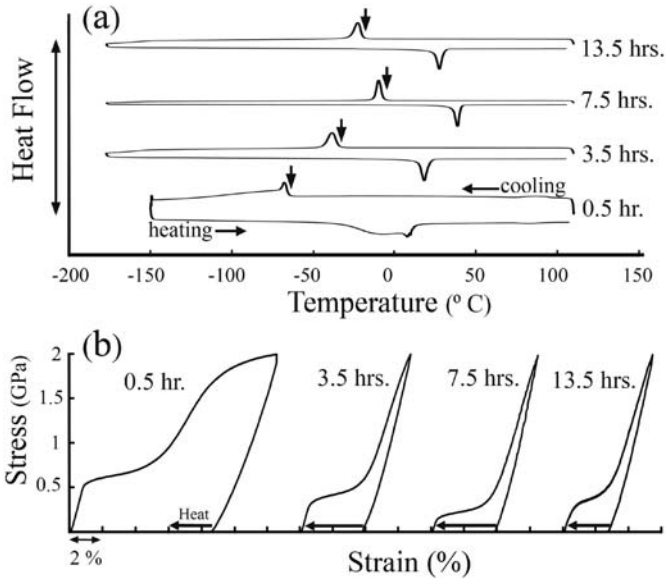

Fig. 1. Effect of aging time at 550 °C on (a) the transformation temperatures and (b) superelastic behavior of $Ni_{50.3}Ti_{41.7}Hf_8$ alloy. M_s is indicated by arrows in each DSC curve.

cycle can be attributed to martensite that did not transform back to austenite. This mechanism was confirmed by heating the samples to 150 °C and measuring the recovered strains, indicated by the solid arrows. For the sample tested above A_f, (the 550 °C/0.5 h sample), only a portion of the strain is recovered upon heating. Thus, much of the unrecovered strain in this sample is due to plastic deformation, as has been documented using neutron diffraction in binary NiTi [20].

It is clear from Fig. 1b that the stress required to form martensite (the plateau stress) first decreases from 650 MPa (550 °C/0.5 h sample) to 420 MPa (550 °C/3.5 h sample), then further drops to 240 MPa (550 °C/7.5 h sample), and then increases back to 370 MPa after aging for 13.5 h. The change in critical martensitic stress with aging time for $Ni_{50.3}Ti_{41.7}Hf_8$ is consistent with the trend in M_s as shown in Fig. 1a. When the M_s decreases, the critical stress for martensitic transformation increases, and vice versa.

Fig. 2a shows the conventional bright field (BF) image of the $Ni_{50.3}Ti_{41.7}Hf_8$ alloy after aging at 550 °C for 0.5 h. The corresponding selected area diffraction pattern (SADP) from the upper grain is also shown in the upper right inset. The main spots in the SADP belong to the B2 cubic austenite structure, and the super reflections at 1/3 positions along $\langle 110\rangle_{B2}$, indicated by arrowheads, are reflections from uniquely oriented H-phase precipitates. The morphology of the H-phase precipitates is shown in an HRTEM micrograph in Fig. 2b (indicated with the letter "P"), and the corresponding FFT is shown in the upper right inset of Fig. 2b. The precipitates (550 °C/0.5 h) are ellipsoidal in shape with average dimensions of 8.4 ± 1 nm (length) and 5.1 ± 1 nm (width); the average interparticle distance is 5 ± 2 nm. Further aging at 550 °C for 3.5 h enlarges the precipitate size to 15 ± 2 nm in length and 7.7 ± 1 nm in width and increases the average interparticle distance to 8 ± 1.5 nm. The average precipitate size and interparticle distance keep increasing with further aging at 550 °C; for a 550 °C/13 h sample, the precipitate size reaches 21 ± 2.5 nm in length and 8.5 ± 1 nm in width, and the average interparticle distance reaches 13 ± 1.5 nm. The average dislocation density was also measured using HRTEM images for $Ni_{50.3}Ti_{41.7}Hf_8$ samples aged at 550 °C for different times, and no changes were observed ($6.5 \pm 0.5 \times 10^{15}/m^2$); therefore, longer aging time 550 °C did not change average dislocation density compared with 550 °C/0.5 h sample. Hence, dislocation annihilation during aging at 550 °C can be excluded as a possible mechanism that influences the transformation stresses and temperatures by further aging the $Ni_{50.3}Ti_{41.7}Hf_8$ alloy at 550 °C.

Fig. 3a and b show the HRTEM and corresponding GPA map (ε_{xx} strain component) of $Ni_{50.3}Ti_{41.7}Hf_8$ after aging at 550 °C for 3.5 h. It is clear from Fig. 3b that the H-phase–matrix interface is still coherent. To accommodate the lattice mismatch, the surrounding matrix is strained up to 2.5% (indicated by white arrows in Fig. 3b) up to 12 nm away from the precipitate–matrix interface; however, with further aging at 550 °C for 13.5 h (Fig. 3c, d), precipitates lose their coherency, and the strain field around the interface is relaxed by formation of misfit dislocations (misfit dislocations are shown by white arrowheads in Fig. 3d). It is worth mentioning that due to the narrow strain field (<2 nm spatial resolution of GPA) around the very fine precipitates (<8 nm in length) after aging at 550 °C for 0.5 h, the GPA did not reveal a strain field. Thus, it can be concluded that the strain field around the H-phase precipitates at the early stage of aging at 550 °C is very narrow, <2 nm. However, as the precipitates increase in size (after aging at 550 °C for 3.5 h), a strain of 2.5% along ε_{xx} can be found as far as 12 nm from the precipitate. Finally, with further aging at 550 °C (13.5 h), the strain field is relaxed by the formation of misfit dislocations.

By concurrently considering the microstructure observations, nanoscale strain field measurements, transformation temperatures, and the macroscopic martensite formation stresses, different mechanisms affecting martensitic transformation in $Ni_{50.3}Ti_{41.7}Hf_8$ can be better explained. It is already known that when the critical size for the nucleation of martensite is larger or comparable to the interparticle distance, the nucleation of martensite can be suppressed [2]. With further aging of $Ni_{50.3}Ti_{41.7}Hf_8$ at 550 °C, average interparticle distance increases from 5 ± 2 nm (0.5 h aging) to 13 ± 2 nm (13.5 h aging), which favors the martensitic transformation. Additionally, because the Ni content of the matrix decreases with increasing volume fraction of precipitate phase [2,9], an increase in M_s with increasing precipitate size should also be expected until the maximum volume fraction of H-phase is reached [2]. Thus, with further aging at 550 °C, one can expect M_s to increase until it reaches a plateau value as reported in references [2,9] for $Ni_{50.3}Ti_{34.7}Hf_{15}$ and $Ni_{50.3}Ti_{29.7}Hf_{20}$ alloys, respectively.

However, as shown in Fig. 1, the M_s increases until an aging time of 7.5 h and then decreases after aging for 13.5 h. This behavior was not previously reported because of the convention of selecting aging time increments based on a log scale instead of a linear scale [2,9]. This decrease in transformation temperature can be explained by the relaxation of strain fields around the precipitates. Normally, transformation temperatures increase when the stress fields are oriented correctly to nucleate the martensite and enough space is provided between precipitates for the nucleation to occur. Until 7.5 h of aging, all the mentioned parameters (i.e., decrease in the Ni content in the matrix, increase in interparticle distance, and increase in the strain field around precipitates)

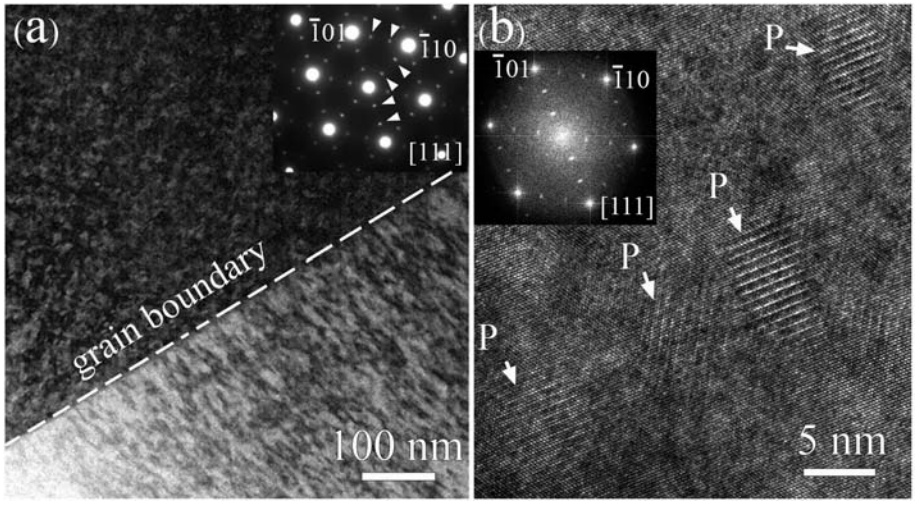

Fig. 2. (a) Conventional BF and corresponding selected area diffraction pattern of the $Ni_{50.3}Ti_{41.7}Hf_8$ alloy after aging at 550 °C for 0.5 h. (b) HRTEM micrograph taken along [111] zone axis showing the H-phase precipitates (indicated by "P") in B2 austenite matrix in $Ni_{50.3}Ti_{41.7}Hf_8$ alloy.

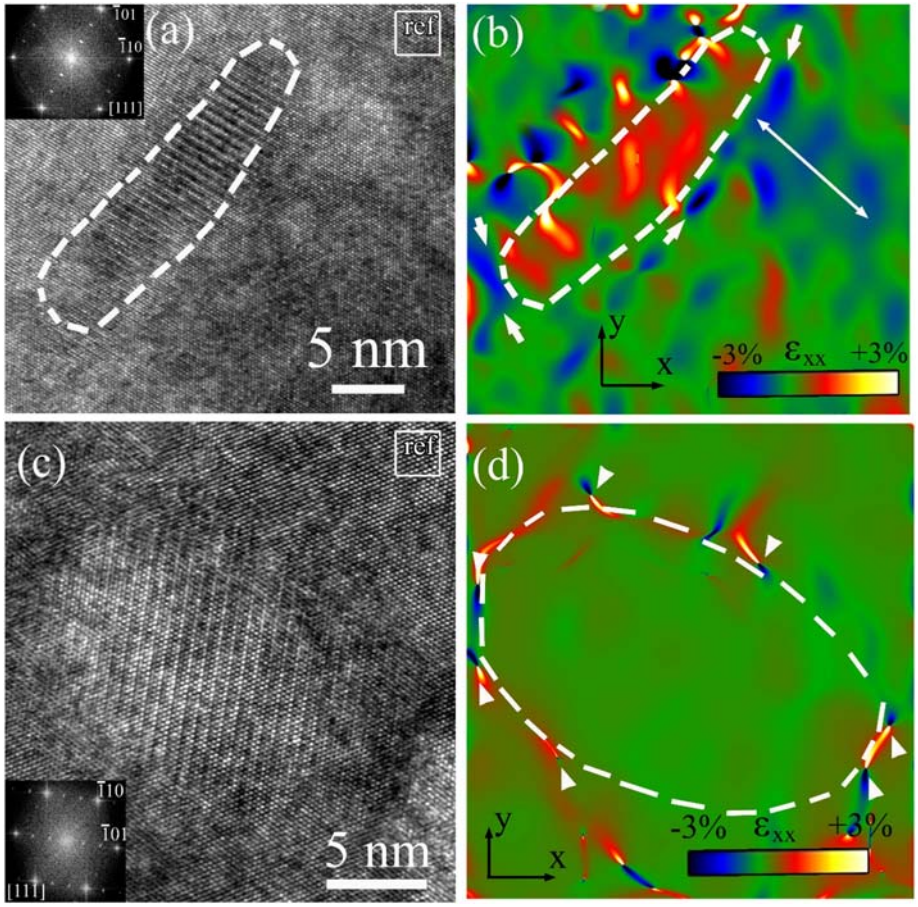

Fig. 3. HRTEM micrograph taken along $[111]_{B2}$ zone axis showing H-phase precipitate and corresponding GPA map of ε_{xx} component in $Ni_{50.3}Ti_{41.7}Hf_8$ alloy after aging at 550 °C for (a,b) 3.5 h and (c,d) 13.5 h. The unstrained region as a reference structure for GPA analysis is also indicated by the white squares in (a) and (c).

favor the martensitic transformation. Beyond 7.5 h aging time, however, the martensitic transformation becomes less favored, because compositional and interparticle effects have begun to saturate and the effect of strain fields have become less favorable. Therefore, of the times we studied, the critical time for aging $Ni_{50.3}Ti_{41.7}Hf_8$ at 550 °C is 7.5 h. At this point, most of the H-phase precipitates are coherent with a high strain field (around 2.5%), and the interparticle distance is high enough to allow nucleation of martensite. However, with further aging for 13.5 h, the precipitates are beginning to lose their coherency and become semi-coherent by forming misfit dislocations, and as a result, the strain fields in the matrix are beginning to relax, ultimately resulting in a decrease in M_s.

In summary, the microstructure, superelasticity, and transformation temperatures in $Ni_{50.3}Ti_{41.7}Hf_8$ alloy after aging at 550 °C for different times were studied. Nano-sized ellipsoidal-shaped H-phase precipitates formed during heat treatment at 300 °C and coarsen after aging at 550 °C. Aging at 550 °C for different times provides a wide range of flexibility in modifying the transformation temperatures and critical martensitic stress. The M_s temperature first increased when aged at 550 °C for 7.5 h and then decreased at higher time. Accordingly, the critical martensitic plateau stress first decreased and then increased. The measurement of the strain field around the precipitates using the GPA technique showed strains up to 2.5% at distances up to 12 nm away from the precipitate–matrix interface which favors the martensitic transformation, however after aging for 13.5 h, most of the precipitates become semi-coherent, resulting in a relaxation of the strain fields and ultimately resulting in the decrease in M_s. Therefore, the coherency of the precipitates plays an important role in controlling the transformation temperatures and stresses of these alloys.

Acknowledgements

B.A. was supported by a fellowship from Confluent Medical Technologies. A.P.S. acknowledges support from the Department of Energy, Basic Energy Sciences (grant no. DE-SP0022534). R.D.N. gratefully acknowledges support from the NASA Transformative Aeronautics Concepts Program, Transformational Tools & Technologies (TTT) Project and the SMA Technology Lead, Othmane Benafan.

References

[1] F. Yang, D.R. Coughlin, P.J. Phillips, L. Yang, A. Devaraj, L. Kovarik, R.D. Noebe, M.J. Mills, Acta Mater. 61 (2013) 3335–3346.
[2] A. Evirgen, I. Karaman, R. Santamarta, J. Pons, R.D. Noebe, Acta Mater. 83 (2015) 48–60.
[3] B. Amin-Ahmadi, T. Gallmeyer, J.G. Pauza, T.W. Duerig, R.D. Noebe, A.P. Stebner, Scr. Mater. 147 (2018) 11–15.
[4] R. Santamarta, F. Arróyave, J. Pons, A. Evirgen, I. Karaman, H.E. Karaca, R.D. Noebe, Acta Mater. 61 (2013) 6191–6206.
[5] X. Meng, W. Cai, K.T. Lau, L.M. Zhou, L. Zhao, J. Mater. Sci. Technol. 22 (2006) 691–695.
[6] X. Meng, W. Cai, Y. Zheng, Y.J. Zhao, Mater. Sci. Eng. A 438-440 (2006) 666–670.
[7] X. Han, R. Wang, Z. Zhang, D. Yang, Acta Mater. 46 (1997) 273–281.
[8] H.E. Karaca, S.M. Saghaian, G. Ded, H. Tobe, B. Basaran, H.J. Maier, R.D. Noebe, Y.I. Chumlyakov, Acta Mater. 61 (2013) 7422–7431.
[9] B.C. Hornbuckle, T.T. Sasaki, G.S. Bigelow, R.D. Noebe, M.L. Weaver, G.B. Thompson, Mater. Sci. Eng. A 637 (2015) 63–69.
[10] G.S. Bigelow, A. Garg, S.A. Padula, D.J. Gaydosh, R.D. Noebe, Scr. Mater. 64 (2011) 725–728.
[11] O. Benafan, R.D. Noebe, S.A. PadulaII, R. Vaidyanathan, Metall. Mater. Trans. A 43 (2012) 4539–4552.
[12] O. Benafan, A. Garg, R.D. Noebe, G.S. Bigelow, S.A. Padula, D.J. Gaydosh, N. Schell, J.H. Mabe, R. Vaidyanathan, Intermetallics 50 (2014) 94–107.
[13] D.R. Coughlin, P.J. Phillips, G.S. Bigelow, A. Garg, R.D. Noebe, M.J. Mills, Scr. Mater. 67 (2012) 112–115.

[14] A.P. Stebner, G.S. Bigelow, J. Yang, D.P. Shukla, S.M. Saghaian, R. Rogers, A. Garg, H.E. Karaca, Y. Chumlyakov, K. Bhattacharya, R.D. Noebe, Acta Mater. 76 (2014) 40–53.
[15] E. Acar, H.E. Karaca, B. Basaran, F. Yang, M.J. Mills, R.D. Noebe, Y.I. Chumlyakov, Mater. Sci. Eng. A 573 (2013) 161–165.
[16] W. Tirry, D. Schryvers, Nat. Mater. 8 (2009) 752–757.
[17] K. Gall, H. Sehitoglu, Y.I. Chumlyakov, I.V. Kireeva, H.J. Maier, J. Eng. Mater. Technol. 121 (1999) 19–27.
[18] D. Schryvers, W. Tirry, Z.Q. Yang, Mater. Sci. Eng. A 438–440 (2006) 485–488.
[19] M.J. Hytch, J.L. Putaux, J.M. Penisson, Nature 423 (2003) 270–273.
[20] A.R. Pelton, B. Clausen, A.P. Stebner, Shape Mem. Superelast. 1 (2015) 375–386.